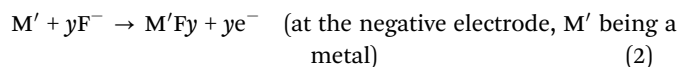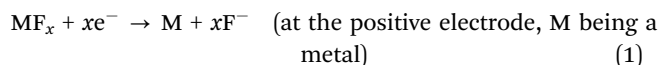ROYAL SOCIETY
OF CHEMISTRY

PAPER

Check for updates

Evolution of fluoride shuttle battery reactions and three-dimensional morphology changes of BiF₃ microparticles in an ethylene carbonate-based liquid electrolyte†

Toshiro Yamanaka, [iD] *[a] Zempachi Ogumi[a] and Takeshi Abe[b]

Fluoride shuttle batteries (FSBs) use defluorination of metal fluorides and fluorination of metals, and they are considered as candidates of next-generation batteries with high energy densities. During FSB reactions of orthorhombic and cubic BiF₃ (o-BiF₃ and c-BiF₃, respectively) in an ethylene carbonate-based liquid electrolyte, *in situ* Raman mapping and *in situ* laser scanning confocal microscopy (LSCM) for three-dimensional analysis were conducted almost simultaneously. As the potential of o-BiF₃ *vs.* Pb (E_{WE}) was decreased to 0.4 V, desorption of F⁻ started at the protrusions of o-BiF₃ particles. After defluorination, E_{WE} was increased to 0.6 V, and c-BiF₃ appeared at protrusions of the surfaces of Bi. However, at the surfaces where o-BiF₃ partially remained, o-BiF₃ grew rather than c-BiF₃. The apparent volumes of particles increased during defluorination and fluorination. The results are important for determining reaction mechanisms, and the results indicate the possibility of the use of ethylene carbonate-based liquid electrolytes.

Introduction

The development of next-generation batteries with high energy density is required for the establishment of a sustainable society with efficient use of energies and with low CO_2 emission. Fluoride shuttle batteries (FSBs), in which fluoride or fluoride ions carry charges between an anode and a cathode, are considered as candidates for future batteries with high energy densities, and they have been extensively studied.[1–24] Defluorination of metal fluorides and fluorination of the resultant metals described below are often used as battery reactions.

$$MF_x + xe^- \rightarrow M + xF^- \quad \text{(at the positive electrode, M being a metal)} \quad (1)$$

$$M' + yF^- \rightarrow M'Fy + ye^- \quad \text{(at the negative electrode, M' being a metal)} \quad (2)$$

Initial examples of rechargeable FSBs are all solid state types, in which a solid electrolyte was used at an elevated temperature of 150 °C to increase ionic conductivity.[3,4] Then the use of several

liquid electrolytes for FSBs at room temperature was demonstrated, showing charging[5] and charge–discharge cycles of FSBs[6] and defluorination–fluorination cycles of single electrodes.[10,11,15] As solvents in these electrolytes, an ionic liquid,[6] glymes,[8–11,16–19] siloxane,[20] γ-butyrolactone[21] and partially fluorinated ether[15] were used. It is difficult to dissolve fluoride sources in many organic solvents. Thus, LiBOB[17] or LiPF₆[8,16,19] was dissolved in glymes to enhance the solubility of CsF (a fluoride source). Anion acceptors were also added to glymes[9–11] and siloxane[20] to dissolve CsF. It is also difficult to develop electrolytes with wide potential windows for using active materials, such as AlF₃ and CeF₃, with low oxidation/reduction potential close to Li⁺/Li (AlF₃: about 0.8 V *vs.* Li⁺/Li, CeF₃: about 0.15 V *vs.* Li⁺/Li), although such electrolytes have been developed for Li ion batteries using ethylene carbonate that forms solid electrolyte interphases (SEI) during its reduction at negative electrodes,[25–27] which are a stable and ionic-conductive surface films that prevent further reduction of the electrolytes.

It is important to study the evolution of FSB reactions and changes in the morphology of active materials during the reactions by using *in situ* methods in order to develop better electrolytes and electrodes. Raman spectroscopy has often been used for studies on battery reactions.[28,29] We have conducted *in situ* Raman spectroscopy during battery reactions including FSB reactions.[16,30–36] Recently, *in situ* Raman mapping was conducted almost simultaneously with *in situ* three-dimensional (3D) morphology analysis by laser scanning confocal microscopy (LSCM) and the method was found to be a

[a] *Office of Society-Academia Collaboration for Innovation, Kyoto University, Gokasho, Uji, Kyoto 611-0011, Japan. E-mail: yamanaka.toshiro.8n@kyoto-u.ac.jp*

[b] *Graduate School of Global Environmental Studies, Kyoto University, Katsura, Nishikyo, Kyoto 615-8510, Japan*

† Electronic supplementary information (ESI) available: Experimental details, ionic conductivity of the electrolyte, height profiles of particles, CV measurements of the electrolyte. See DOI: https://doi.org/10.1039/d2ya00184e

powerful method for determining reaction mechanisms and rate-determining steps.[36]

In the present work, evolution of FSB reactions of orthorhombic and cubic BiF_3 (o-BiF_3 and c-BiF_3), respectively (see Fig. 1(a) and (b)) microparticles partly embedded in a gold plating film (o-BiF_3/gold and c-BiF_3/gold, respectively, see Fig. 1(c)) in an ethylene carbonate-based electrolyte (tetramethylammonium fluoride (TMAF) dissolved in ethylene carbonate and diethyl carbonate (ECDEC)) was studied by *in situ* Raman mapping and *in situ* analysis of 3D morphology and colors by laser scanning confocal microscopy (LSCM). FSB reactions were found to proceed in the electrolyte, suggesting the possibility of future developments of ethylene carbonate-based electrolytes for FSBs with wide potential windows and with various breakthroughs. During fluorination after complete defluorination of o-BiF_3, c-BiF_3 appeared at protruded positions at the surfaces of pure Bi. On the other hand, o-BiF_3 grew rather than c-BiF_3 in the areas where Bi and partially remaining o-BiF_3 coexisted, suggesting that o-BiF_3 acted as nuclei for fluorination. The results also suggest that the rate-determining step of fluorination of pure Bi to form c-BiF_3 is incorporation of F^- from the electrolyte into Bi.

Experimental

o-BiF_3 microparticles were supplied by Fluorochem Ltd. c-BiF_3 microparticles were prepared by annealing o-BiF_3 microparticles at 150 °C in vacuum for 12 hours.[34,35] Structures of o-BiF_3 and c-BiF_3 are shown in Fig. 1(a) and (b), respectively. The o-BiF_3 and c-BiF_3 particles were embedded in a gold plating film on a gold foil to make o-BiF_3/gold and c-BiF_3/gold, respectively (see Section S1 in ESI† and ESI of ref. 32 for details). Briefly, a gold foil (Nilaco Corporation, 99.95% pure, 0.2 mm in thickness) was put in a gold plating solution for deposition of 24 K gold (Marui Galvanizing Co. Ltd) in a glass tube. A small amount of o-BiF_3 or c-BiF_3 powder were then put in the solution. A platinum wire was inserted in the solution and a current was applied between the wire and the gold foil for deposition of gold. The amount of deposited gold corresponded to that of the gold plating film with a thickness of 2 μm without BiF_3. The resultant o-BiF_3/gold and c-BiF_3/gold were washed with pure water and dried.

An electrolyte was prepared in an Ar atmosphere in a glove box by dissolving about 0.08 M (saturation) of TMAF (Kumidas Co., Ltd) in ECDEC (EC:DEC = 1:1) (Kishida Chemical Co., Ltd). The ionic conductivity of the electrolyte was 4.2×10^{-3} S cm^{-1} at 25 °C (see Section S2 in ESI†).

Electrochemical cells were assembled in the glove box. The details of the cells are described in Section S1 in ESI† and ESI of ref. 36. The cell had a quartz window and a Pb wire as a counter electrode. The distance between the surface of the gold plating film and the quartz window was about 15 μm, and the gap between them was filled with the electrolyte. The cell was sealed with Kalrez and it was placed in an Ar flow during *in situ* Raman mapping and *in situ* LSCM measurements. The open circuit
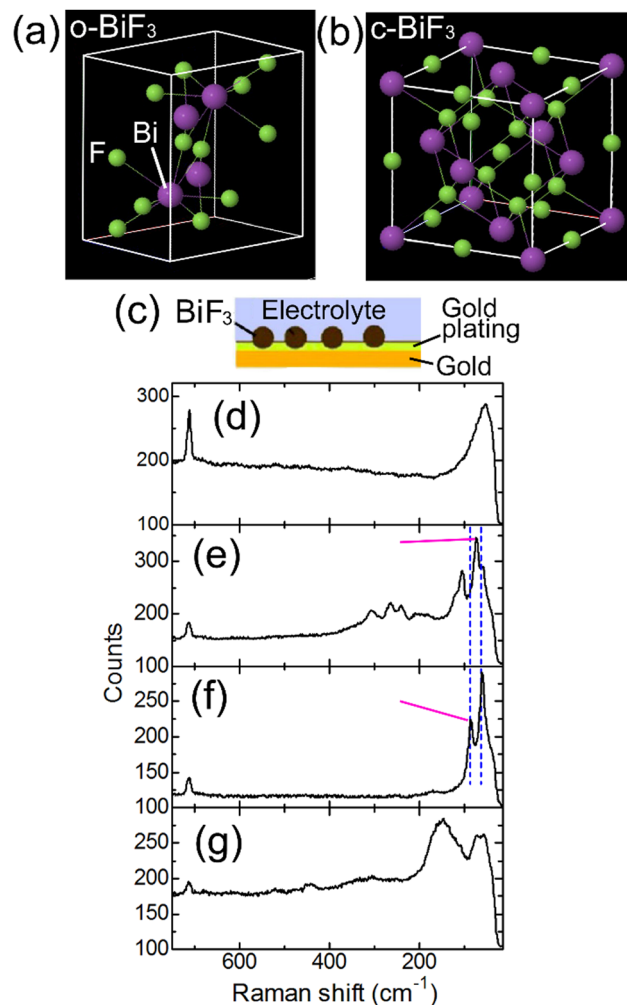

Fig. 1 Structures of o-BiF_3 and c-BiF_3 and Raman spectra of o-BiF_3/gold and c-BiF_3/gold samples in electrochemical cells. (a) and (b) show structures of o-BiF_3 and c-BiF_3, respectively. (c) shows an illustration of an o-BiF_3/gold or a c-BiF_3/gold sample. (d) and (e) show Raman spectra obtained at the positions of the gold substrate and an o-BiF_3 particle on an o-BiF_3/gold sample in a cell before defluorination, respectively. (f) shows a Raman spectrum obtained at the position of a particle on the o-BiF_3/gold sample in the cell after defluorination. (g) shows a Raman spectrum obtained at the position of a particle on a c-BiF_3/gold sample in another cell before defluorination.

voltage (OCV) was typically 0.55 V. FSB reactions were induced by changing the potential of BiF_3/gold *vs.* the Pb reference electrode (E_{WE}).

In situ Raman mapping was conducted with an NRS-4500 Raman spectrometer (JASCO Corporation) and 532 nm laser light. It typically took 16 minutes for mapping of areas of 45 μm (150 points) × 50 μm (150 points).

In situ 3D analysis of morphologies of o-BiF_3 and c-BiF_3 microparticles at the surfaces of o-BiF_3/gold and c-BiF_3/gold samples was conducted by using LSCM (VK-X1000/1100, Keyence Corporation). Raman mapping and LSCM measurements were conducted by placing the cell on the sample stages of the Raman and LSCM apparatuses in turn without interrupting Ar flow and FSB reactions. Raman mapping was conducted for

several areas (16 minutes for one area) and then the cell was transferred to the LSCM apparatus to analyze 3D morphologies for the areas. Accurate positioning after transfer of the cell between the two apparatuses took some time. Therefore, the timing of Raman mapping and that of LSCM measurements differed by 30 minutes to two hours.

Results and discussion

An electrochemical cell was constructed using an o-BiF$_3$/gold sample. Fig. 1(d) and (e) show Raman spectra taken at the positions of the gold substrate and an o-BiF$_3$ particle in the cell, respectively (see Fig. 1(c)). The peak at 715 cm^{-1} in Fig. 1(d) is assigned to the symmetric ring deformation mode of EC.[37,38]

The peak at 52 cm^{-1} was not previously reported because this peak is out of the wavenumber ranges in previous papers, and it is thought to be Raman scattering from the electrolyte. The two clear peaks at 73 cm^{-1} and 105 cm^{-1} and small peaks from 150 cm^{-1} to 340 cm^{-1} in Fig. 1(e) are scattering from o-BiF$_3$.[39] After defluorination, Raman scattering of Bi appeared at 60 cm^{-1} and 85 cm^{-1} (Fig. 1(f)) as indicated by blue dashed lines.[40–42] In the following, mappings of the areas of the peaks at 73 cm^{-1} (o-BiF$_3$) and 85 cm^{-1} (Bi) indicated by red-violet lines are shown.

To induce defluorination of o-BiF$_3$, E_{WE} was decreased from OCV (0.55 V) to 0.2 V step by step as shown in Fig. 2(a), and the current shown in Fig. 2(b) appeared. Fig. 2(c) shows CCD (Charge-Coupled Device) images of o-BiF$_3$/gold in the cell after keeping E_{WE} at 0.4 V for 1 hour taken by a CCD camera of the Raman apparatus, Raman mapping of the areas of the peaks for o-BiF$_3$ and Bi, and superposition of the CCD image and the mapping for Bi. The distribution of o-BiF$_3$ coincides with that of dark areas in the CCD image, indicating that the dark areas are o-BiF$_3$ particles. Bi had already appeared at some parts of the surfaces of o-BiF$_3$ particles, indicating that defluorination had occurred at these parts, as shown by the mapping for Bi. After the o-BiF$_3$/gold was kept at 0.4 V for 5 hours, defluorination further proceeded as shown in the mappings for Bi and o-BiF$_3$ in Fig. 2(d), in which the areas of the peak for Bi increased at some positions and those for o-BiF$_3$ at the corresponding positions decreased. In the CCD image in Fig. 2(d), contrasts of the particles became dark at the positions where defluorination proceeded, indicating that the dark contrasts correspond to Bi.

Fig. 3 shows results of *in situ* LSCM measurements of the same area as that of Raman mapping shown in Fig. 2. Fig. 3(a) and (b) show results at OCV just before E_{WE} was changed to 0.4 V and after E_{WE} was kept at 0.4 V for 6 hours, respectively, the timings of which are close (within 1 hour difference) to those of Raman mapping shown in Fig. 2(c) and (d), respectively. The upper and lower panels of Fig. 3(a) and (b) show confocal CCD images and results of 3D analysis, respectively. In the confocal CCD images, all positions on the substrate surface and the protruding surfaces of particles in focus, resulting in clearer images than the CCD images taken by the Raman apparatus shown in Fig. 2(c) and (d) in which the focus was
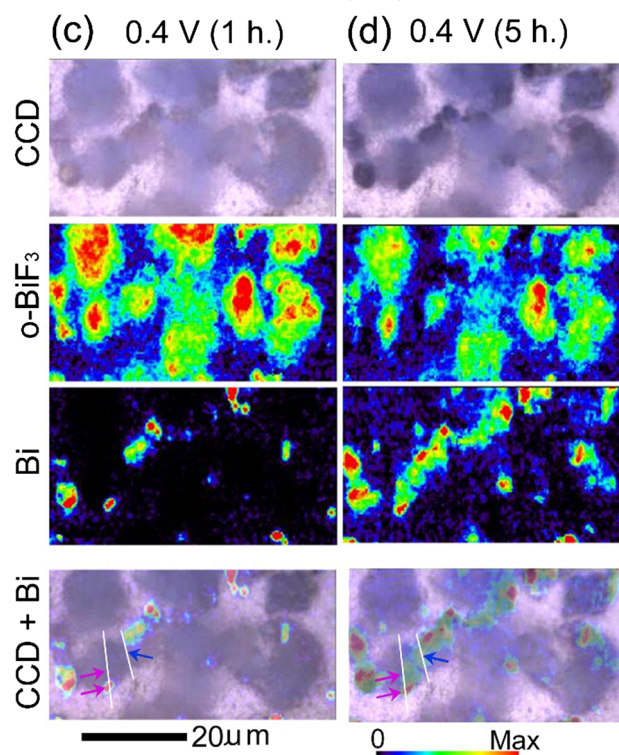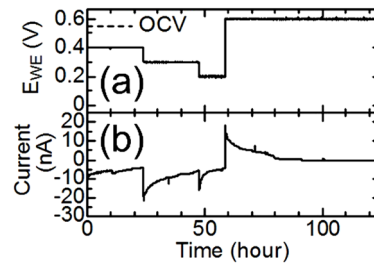

Fig. 2 *In situ* Raman mapping of o-BiF$_3$/gold during defluorination: (a) and (b) show the voltage applied to induce defluorination and the current that appeared, respectively. (c) and (d) show results after E_{WE} was kept at 0.4 V for 1 hour and at 0.4 V for 5 hours, respectively. CCD images, mappings of areas of the peaks for o-BiF$_3$ and Bi, and superposition of the CCD images and the mappings for Bi are shown. The red-violet and blue arrows in the superposition images indicate positions where defluorination started (nuclei of Bi appeared). Height profiles along white lines in the superposition images are shown in Fig. 3(c) and (d).

adjusted to the substrate surface and the protruding surfaces of the particles are therefore out of focus. In the confocal CCD image in Fig. 3(b), some parts of the particles, such as the positions indicated by blue and red-violet arrows, became darker than the corresponding positions in the image in Fig. 3(a), indicating that defluorination started at these positions. The 3D morphology in Fig. 3(b) did not change significantly compared with that in Fig. 3(a). Height profiles along lines A, B and C, D in Fig. 3(b), which include the positions indicated by the blue and red-violet arrows, respectively, are shown in Fig. 3(c) and (d), respectively. The positions indicated by the blue and red-violet arrows in Fig. 3(c) and (d) correspond to those in Fig. 3(b), respectively. It can be seen that there are protrusions at these positions, suggesting that defluorination
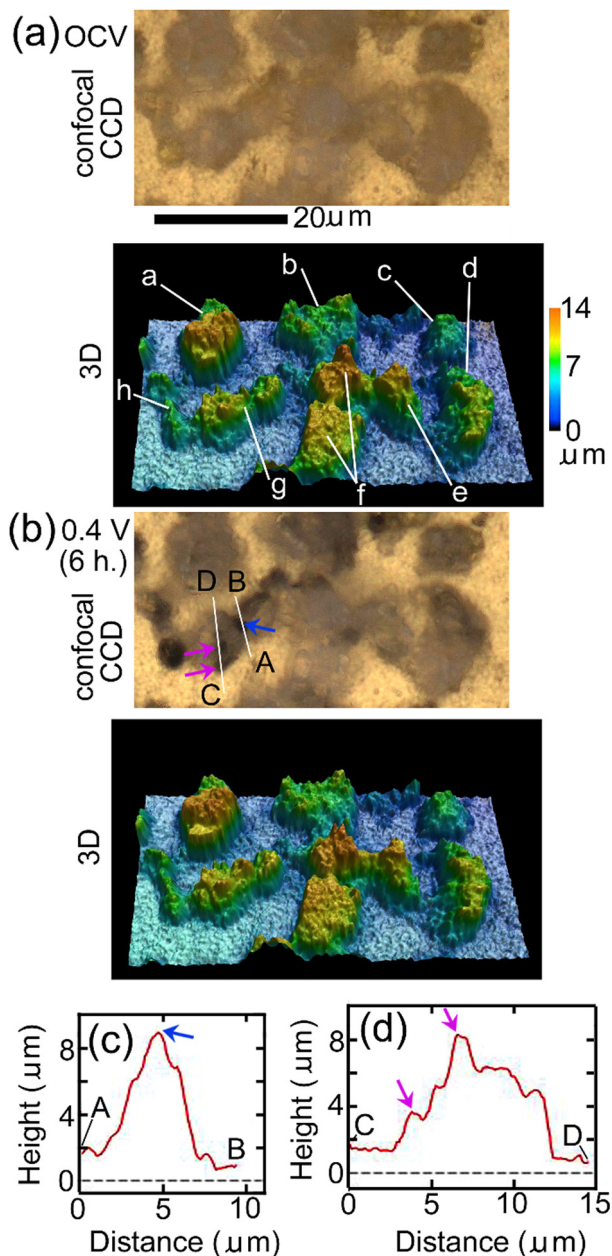
Fig. 3 *In situ* 3D morphology analysis of o-BiF$_3$/gold during defluorination: (a) and (b) show confocal CCD images and 3D morphology at OCV and after E_{WE} was kept at 0.4 V for 6 hours, respectively. (a)–(h) Indicate particles of which apparent volumes above gold during defluorination and fluorination were analyzed as shown later. The contrasts of the positions indicated by blue and red-violet arrows in (b) became dark compared with those of corresponding positions in (a). (c) and (d) show height profiles along lines A, B and C, D in (b). Blue and red-violet arrows in (c) and (d) correspond to the positions indicated by blue and red-violet arrows in (b).

by desorption of F$^-$ started at the positions with small radii of curvatures where electric fields are strong and that the rate-determining step of defluorination of large o-BiF$_3$ particles by desorption of F$^-$ is extraction of F$^-$ from the surface of o-BiF$_3$ into the electrolyte. Such phenomena are observed in defluorination of PbF$_2$[36] and BiF$_3$[35] in different electrolytes. Generally, an electric field at an interface between an electrolyte and the

surface of an active material is strong when the radius of curvature of the surface is small, which promotes an electrochemical reaction, as is often observed by dendrite formation in electrodeposition of Li and Zn.[43,44] Height profiles at additional different positions also suggest that defluorination started at protrusions (see Section S3 in ESI†).

E_{WE} was decreased to 0.2 V to further promote defluorination. Fig. 4(a) shows CCD images, Raman mapping of the areas of the peaks for o-BiF$_3$, c-BiF$_3$ and Bi, and superposition of the CCD image and the mapping for c-BiF$_3$ after o-BiF$_3$/gold was kept at 0.2 V for 10 hours. The peak of c-BiF$_3$ at 150 cm^{-1} was used for mapping for c-BiF$_3$ (see the spectrum in Fig. 1(g) that was obtained at the position of a particle on a c-BiF$_3$/gold sample in another electrochemical cell.) The contrasts of particles became dark and the areas of the peak for Bi increased, indicating that defluorination of the surfaces of the particles was almost completed. However, Bi and small amounts of remaining o-BiF$_3$ co-existed on the particles indicated by c (only contours of the particle), d and e in the CCD image in Fig. 4(a), as shown by the mappings for o-BiF$_3$ and Bi in Fig. 4(a). Then E_{WE} was increased to 0.6 V to induce fluorination, and Raman and LSCM measurements were conducted during the fluorination processes. Fig. 4(b) and (c) show results after E_{WE} was kept at 0.6 V for 18 hours and 50 hours, respectively. It can be seen that o-BiF$_3$ grew at surfaces of particles c, d and e, where o-BiF$_3$ and Bi co-existed before E_{WE} was changed to 0.6 V. On the other hand, c-BiF$_3$ grew at surfaces of particles at the center and the left side of which the surfaces were covered with only Bi before E_{WE} was changed to 0.6 V (Fig. 4(a)). The results indicate that o-BiF$_3$ acts as nuclei in fluorination of Bi to form o-BiF$_3$.

Fig. 5(a)–(c) show results of *in situ* 3D analysis after E_{WE} was kept at 0.2 V for 11 hours, at 0.6 V for 17 hours and at 0.6 V for 48 hours, respectively, the timings of which are close (within 2 hours difference) to those of *in situ* Raman mappings shown in Fig. 4(a)–(c), respectively. In the confocal CCD images in Fig. 5(b) and (c), contrasts of particles became brighter than those in Fig. 5(a), indicating fluorination. It can be seen that the apparent volumes of particles above gold increased during fluorination. (The apparent volume is the volume of a particle defined by the outermost surface of the particle that may have fine spaces (such as pores) inside. The real volume does not include the volumes of the fine spaces and cannot be calculated. Apparent volumes can be calculated by the software attached to the LSCM apparatus.) In the superposition of CCD images and mapping for c-BiF$_3$ in Fig. 4, fluorination of the surface of particles at which only Bi existed is thought to have started at the positions indicated by red-violet lines. These positions correspond to the positions indicated by red-violet arrows in the confocal CCD image in Fig. 5(a). Height profiles along lines A, B and C, D that include the positions of the arrows in Fig. 5(a) are shown in Fig. 5(d) and (e), respectively. Red-violet arrows in Fig. 5(d) and (e) correspond to the positions indicated by the red-violet arrows in Fig. 5(a). It can be seen that there are protrusions at the positions, suggesting that fluorination starts at positions with small radii of curvatures
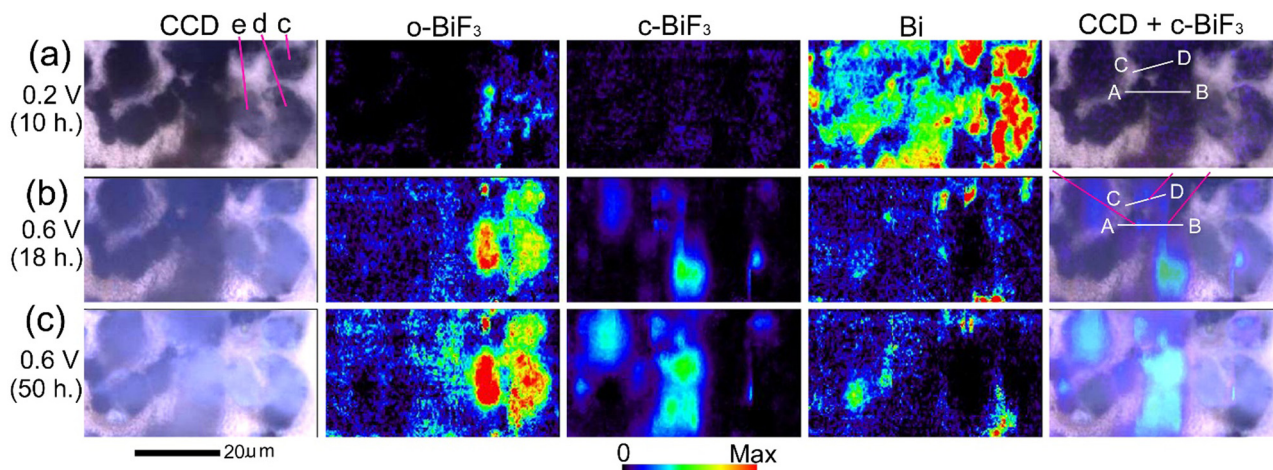
Fig. 4 *In situ* Raman mapping of o-BiF$_3$/gold during fluorination after defluorination: (a), (b) and (c) show results after E_{WE} was kept at 0.2 V for 10 hours, at 0.6 V for 18 hours and at 0.6 V for 50 hours, respectively. CCD images, mappings of areas of the peaks for o-BiF$_3$, c-BiF$_3$ and Bi, and superposition of the CCD images and mappings for Bi are shown. The red-violet lines in the superposition image in (b) indicate positions where fluorination started (nuclei of c-BiF$_3$ appeared). Height profiles along white lines AB and CD in the superposition images are shown in Fig. 5(d) and (e).
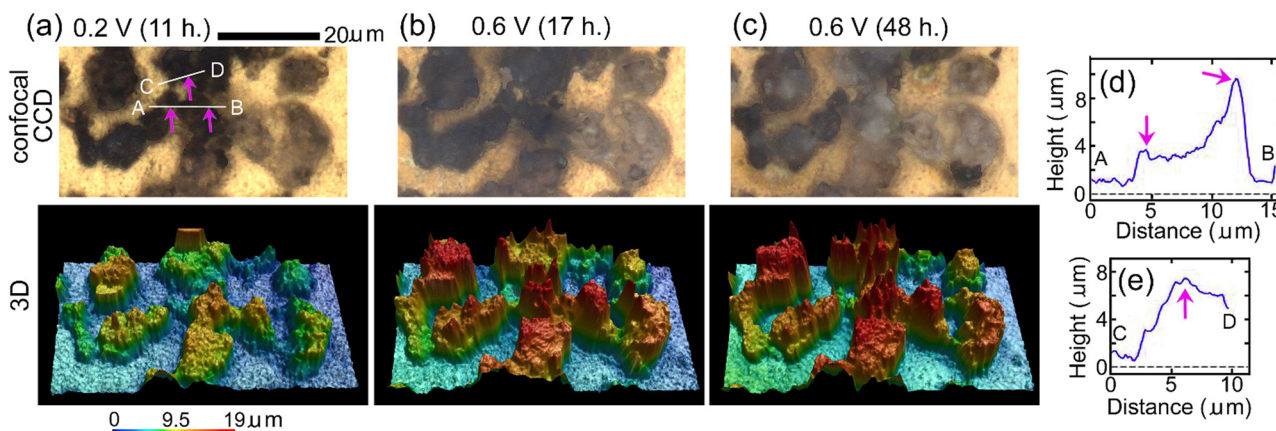

Fig. 5 *In situ* 3D morphology analysis of o-BiF$_3$/gold during fluorination after defluorination: (a), (b) and (c) show confocal CCD images and 3D morphology after E_{WE} was kept at 0.2 V for 11 hours, at 0.6 V for 17 hours and at 0.6 V for 48 hours, respectively. The positions indicated by red-violet arrows in (a) correspond to the positions indicated by red-violet lines in Fig. 4(b) where nuclei of c-BiF$_3$ appeared. (d) and (e) show height profiles along white lines A, B and C, D in (a), respectively. Red-violet arrows in (d) and (e) correspond to the positions indicated by red-violet arrows in (a).

where electric fields are strong. The rate-determining step of fluorination of Bi particles is thought to be incorporation of F$^-$ from the electrolyte to the surface of the particles.

Fig. 6 shows changes in apparent volumes above gold of particles indicated by a–h in Fig. 3(a) during defluorination and fluorination processes shown in Fig. 2–5. It can be seen that apparent volumes of most of the particles increased slightly during defluorination, which is contrary to expectation. During subsequent fluorination, the apparent volumes above gold of the particles increased more clearly, being consistent with expectation. Thus, the apparent volumes of particles after a defluorination–fluorination cycle are larger than their initial values.

Another cell was constructed using a c-BiF$_3$/gold sample, and defluorination of c-BiF$_3$ particles was studied. E_{WE} was

decreased from OCV (0.55 V) to 0.15 V step by step to induce defluorination as shown in Fig. 7(a), and the current shown in Fig. 7(b) appeared. The current at 0.4 V (-43 nA) is larger than that for o-BiF$_3$ (-8.3 nA) (Fig. 2(b)). This may be due to a dark current of unknown side reactions because a higher rate of defluorination of c-BiF$_3$ than that for o-BiF$_3$ was not recognized on the basis of Raman measurements. The current after 2.5 hours in Fig. 7(b) is larger than the current from 22 to 60 hours in Fig. 2(b), which is partly due to the rapid decrease in E_{WE} for c-BiF$_3$ (As shown in Fig. 7(b), E_{WE} decreased to 0.15 V within 5 hours.) compared with that for o-BiF$_3$. (As shown in Fig. 2(b), E_{WE} decreased to 0.2 V over a period of 47 hours.) Fig. 7(c) shows CCD images, Raman mapping of the areas of the peaks for c-BiF$_3$ and Bi, and superposition of the CCD image and the mapping for Bi after c-BiF$_3$/gold was kept at 0.4 V for
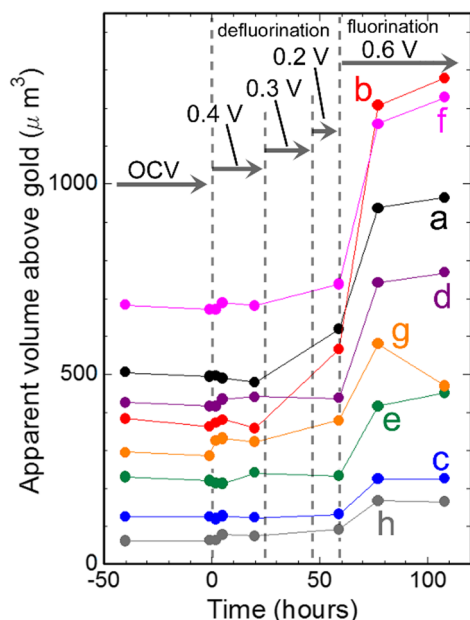
Fig. 6 Changes in apparent volumes of particles indicated by a–h in Fig. 3(a) against time.

1 hour. The existence of Bi in the mapping for Bi indicates that the surfaces of particles had partially defluorinated. After keeping E_{WE} at 0.15 V for 1 hour, the areas of the peaks for Bi and c-BiF$_3$ increased and decreased, respectively, as shown by Fig. 7(d), indicating further defluorination.

Fig. 8(a) and (b) show results of *in situ* 3D analysis conducted after E_{WE} was kept at 0.4 V for 1.5 hours and at 0.15 V for 2.5 hours, respectively, of which timings are close (within 1.5 hours difference) to those of Raman mappings shown in Fig. 7(c) and (d), respectively. In Fig. 7(c), it can be seen that defluorination started at the positions indicated by blue, black and red-violet lines. Corresponding positions in the confocal CCD image in Fig. 8(a) are indicated by blue, black and red-violet arrows. Height profiles along lines A, B and C, D in Fig. 8(a) that include the positions indicated by the arrows are shown in Fig. 8(c) and (d), respectively. The positions indicated by blue, black and red-violet arrows in Fig. 8(c) and (d) correspond to those in Fig. 8(a). There are protrusions in these positions, suggesting that the rate-determining step of defluorination of c-BiF$_3$ particles by desorption of F$^-$ is extraction of F$^-$ from the surface of c-BiF$_3$ into the electrolyte. Height profiles at other positions were also obtained, and the results suggest that defluorination started at protrusions (see Section S4 in ESI†). Changes in apparent volumes above gold of particles indicated by a–g in Fig. 8(a) are shown in Fig. 8(e). Apparent volumes of particles surrounded by a white dashed curve in Fig. 8(a) were not analyzed because the morphologies of the particles changed too much during defluorination, and it was difficult to analyze the apparent volume of each of the particles. It can be seen that apparent volumes increased during defluorination.

In Fig. 6 and 8(e), increases in apparent volumes can be seen during defluorination, which is contrary to expectation.
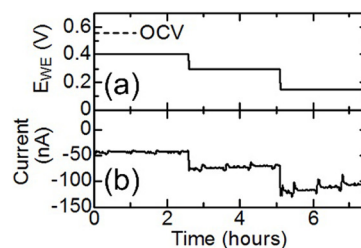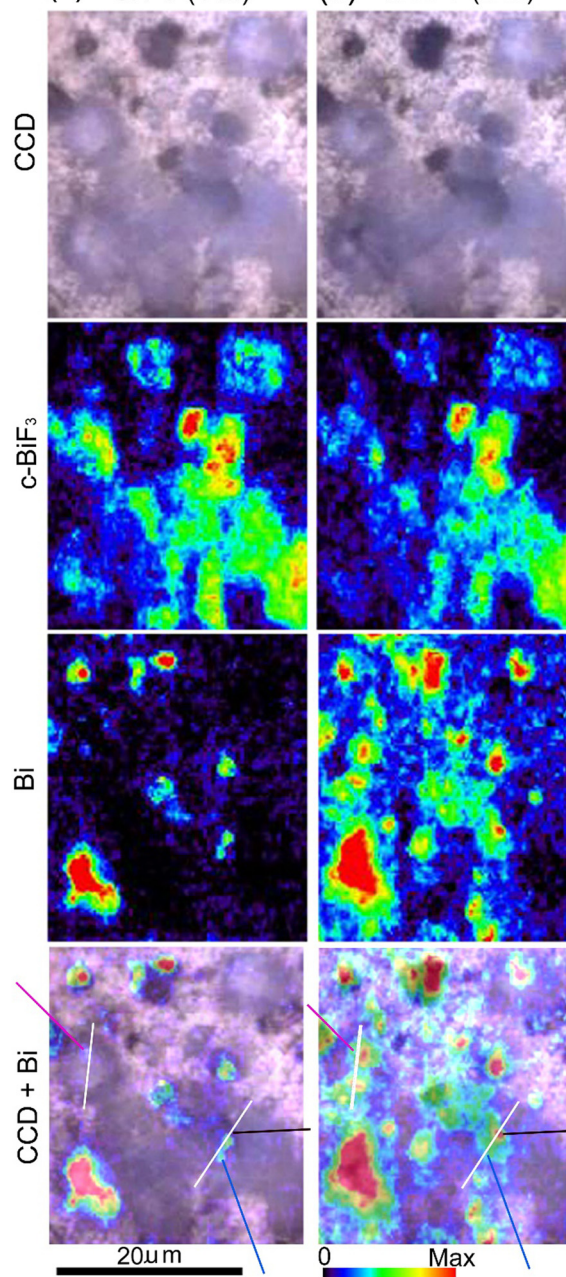

Fig. 7 *In situ* Raman mapping of c-BiF$_3$/gold during defluorination: (a) and (b) show the voltage applied to induce defluorination and the current that appeared, respectively. (c) and (d) show results after E_{WE} was kept at 0.4 V for 1 hour and at 0.15 V for 1 hour, respectively. CCD images, mappings of areas of the peaks for c-BiF$_3$ and Bi, and superposition of the CCD images and the mappings for Bi are shown. The blue, black and red-violet lines in the superposition images indicate positions where defluorination started (nuclei of Bi appeared). Height profiles along white lines in the superposition images are shown in Fig. 8(c) and (d).
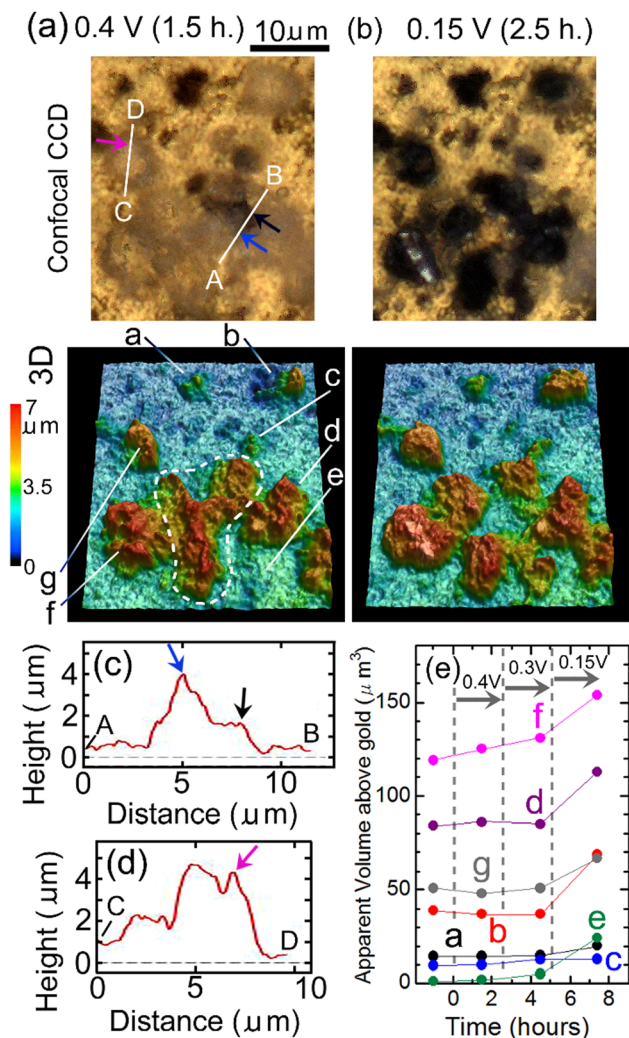
Fig. 8 *In situ* 3D morphology analysis of c-BiF$_3$/gold during defluorination: (a) and (b) show confocal CCD images and 3D morphology after E_{WE} was kept at 0.4 V for 1.5 hours and at 0.15 V for 2.5 hours, respectively. The blue, black and red-violet arrows indicate positions where defluorination started (nuclei of Bi appeared). (c) and (d) show height profiles along lines A, B and C, D in (a), respectively. Blue, black and red-violet arrows in (c) and (d) correspond to the positions indicated by blue, black and red-violet arrows in (a). (e) shows changes in apparent volumes of particles indicated by a–g in (a) against time. Measurements of apparent volumes of particles surrounded by a white dashed curve were difficult due to large morphology changes.

However, clearer increases in apparent volumes were observed during defluorination of PbF$_2$ in a CsF/LiBOB/tetraglyme electrolyte.[36] Therefore, increases in apparent volumes of metal fluorides during defluorination in liquid electrolytes may not be rare phenomena. The density of the resultant Bi should be lower than the densities of initial o-BiF$_3$ and c-BiF$_3$, and structures of the resultant Bi may be dendritic. In the case of PbF$_2$ in the Cs/LiBOB/tetraglyme electrolyte, fluorination was not clearly observed during oxidation because significant desorption of Pb (Pb → Pb^2 + 2e$^-$) occurred, resulting in decreases in apparent volumes of particles. On the other hand, in the present study, fluorination by direct reaction of F$^-$ and Bi

was the main process during oxidation, and desorption of Bi during oxidation was less significant. Thus, increases in the apparent volumes during fluorination were clearly observed, as shown in Fig. 6. After a defluorination/fluorination cycle, the volumes increased compared with the initial values before the cycle. This leads to agglomeration of particles, which leads to loss of capacities of electrodes due to loss of surface areas of active materials when composite electrodes of BiF$_3$ are operated in the present electrolyte. (Desorption of Pb during the fluorination process results in adsorption of Pb during the next defluorination process at, for example, the positions between particles, which also causes agglomeration.) The development of an appropriate fluoride–carbon complex may be needed to prevent agglomeration.

Ethylene carbonate-based electrolytes are used in lithium ion batteries, and wide potential windows of the electrolytes are attained by formation of SEI. It is thought that SEI should contain LiF to achieve good functions of SEI.[27] LiF is produced from components of the electrolytes, *e.g.*, Li$^+$ and PF$_6^-$, during formation of SEI. The electrolyte used in the present study did not contain such effective components, and good SEI will not be obtained when the electrolyte is used for FSBs with negative electrodes (Al, Ce, *etc.*) unless some additives suitable for FSBs are developed. Results of cyclic voltammetry of the TMAF/ECDEC electrolyte (see Section S5 in ESI†) showed that the reduction current around −3 V at the 4th cycle was suppressed compared with that at the 1st cycle, but there was still significant reduction current at the 4th cycle, indicating that good SEI were not formed. Nevertheless, FSB reactions observed in the present study indicate the possibility of the use of ethylene carbonate-based electrolytes for FSBs to achieve wide potential windows in the future.

In lithium ion batteries, LiCoO$_2$ (practical capacity: 160 mA h g^{-1}) and graphite (372 mA h g^{-1}) are used for positive and negative electrodes, respectively, and the voltage is about 3.7 V. If Cu (843 mA h g^{-1}) positive and LaF$_3$ (410 mA h g^{-1}) negative electrodes are used with an ethylene carbonate-based electrolyte in an FSB, the cell voltage will be about 3 V, and the weight energy density of the FSB is expected to be about two-times higher than that of lithium ion batteries. However, in many reports of single electrode tests of FSB reactions with liquid electrolytes, the capacity and the cyclability are far from practical levels.[9–11,15,17,18,21,22] In addition, there have been few reports of rechargeable FSB reactions in a liquid electrolyte using both positive and negative electrodes.[6] Realization of FSBs with high energy densities and high cyclability comparable to those of lithium ion batteries requires many breakthroughs.

Conclusions

In situ Raman mapping and *in situ* LSCM were conducted almost simultaneously in the same areas of samples in turn during FSB reactions of o-BiF$_3$ and c-BiF$_3$ particles in an ethylene carbonate-based electrolyte in order to study changes

in chemical distribution and 3D morphology of the particles. The rate-determining steps of defluorination of o-BiF$_3$ and c-BiF$_3$ particles are thought to be extraction of F$^-$ from BiF$_3$ to the electrolyte. c-BiF$_3$ formed in fluorination of Bi, and the rate-determining step in this process is thought to be incorporation of F$^-$ from the electrolyte to Bi. On the other hand, o-BiF$_3$ grew rather than c-BiF$_3$ during fluorination of surfaces where Bi and o-BiF$_3$ coexisted, suggesting that o-BiF$_3$ acted as nuclei for fluorination. The apparent volumes of particles increased during defluorination and subsequent fluorination. The increases in apparent volumes during defluorination of metal fluorides in liquid electrolytes are thought to be general phenomena. The results will lead to strategies to make better electrolytes and electrodes, and the results also indicate the possibility of using ethylene carbonate-based liquid electrolytes for FSBs.

Conflicts of interest

There are no conflicts to declare.

Acknowledgements

Notes and references

1 F. Gschwind, G. Rodriguez-Garcia, D. J. S. Sandbeck, A. Gross, M. Weil, M. Fichtner and N. Hormann, *J. Fluorine Chem.*, 2016, **182**, 76–90.

2 M. A. Nowroozi, I. Mohammad, P. Molaiyan, K. Wissel, A. R. Munnangi and O. Clemens, *J. Mater. Chem. A*, 2021, **9**, 5980–6012.

3 M. A. Reddy and M. Fichtner, *J. Mater. Chem.*, 2011, **21**, 17059–17062.

4 C. Rongeat, M. A. Reddy, T. Diemant, R. J. Behm and M. Fichtner, *J. Mater. Chem. A*, 2014, **2**, 20861–20872.

5 F. Gschwind, Z. Zao-Karger and M. Fichtner, *J. Mater. Chem. A*, 2014, **2**, 1214–1218.

6 K. Okazaki, Y. Uchimoto, T. Abe and Z. Ogumi, *ACS Energy Lett.*, 2017, **2**, 1460–1464.

7 M. A. Nowroozi, K. Wissel, J. Rohrer, A. R. Munnangi and O. Clemens, *Chem. Mater.*, 2017, **29**, 3441–3453.

8 H. Nakamoto, Z. Ogumi and T. Abe, *Jp. Pat.*, JP6342837, 2018.

9 Z. Ogumi, T. Hirai, J. Yamaki, H. Horino, K. Okazaki and Y. Koyama, *Jp. Pat.*, 2013-270415, 2013.

10 K. Konishi, K. Kono, T. Abe and Z. Ogumi, *Jp. Pat.*, JP2017-10865, 2017.

11 H. Konishi, T. Minato, T. Abe and Z. Ogumi, *J. Electroanal. Chem.*, 2018, **826**, 60–64.

12 A. Grenier, A. G. Porras-Gutierrez, H. Groult, K. Beyer, O. J. Borkiewicz, K. W. Chapman and D. Dambournet, *J. Mater. Chem. A*, 2017, **5**, 15700–15705.

13 I. Mohammad, R. Witter, M. Fichtner and M. A. Reddy, *ACS Appl. Energy Mater.*, 2018, **1**, 4766–4775.

14 M. A. Nowroozi, S. Ivlev, J. Rohrer and O. Clemens, *J. Mater. Chem. A*, 2018, **6**, 4658–4669.

15 V. K. Davis, C. M. Bates, K. Omichi, B. M. Savoie, N. Momčilović, Q. Xu, W. J. Wolf, A. Michael, M. A. Webb, K. J. Billings, N. H. Chou, S. Alayoglu, R. K. McKenney, I. M. Darolles, N. G. Nair, A. Hightower, D. Rosenberg, M. Ahmed, C. J. Brooks, T. F. Miller III, R. H. Grubbs and S. C. Jones, *Science*, 2018, **362**, 1144–1148.

16 T. Yamanaka, H. Nakamoto, T. Abe, K. Nishio and Z. Ogumi, *ACS Appl. Energy Mater.*, 2019, **2**, 3092–3097.

17 A. Celik-Kucuk, T. Minato, T. Yamanaka and T. Abe, *J. Mater. Chem. A*, 2019, **7**, 8559–8567.

18 A. Celik-Kucuk, T. Yamanaka, Y. Yokoyama and T. Abe, *J. Electrochem. Soc.*, 2021, **168**, 010501.

19 S. Kobayashi, H. Nakamoto, D. Yokoe, A. Kuwabara, T. Abe and Y. Ikuhara, *ACS Appl. Energy Mater.*, 2021, **4**, 996–1003.

20 A. Celik Kucuk, T. Yamanaka and T. Abe, *J. Mater. Chem. A*, 2020, **8**, 22134–22142.

21 M. Kawasaki, K.-I. Morigaki, G. Kano, H. Nakamoto, R. Takekawa, J. Kawamura, T. Minato, T. Abe and Z. Ogumi, *J. Electrochem. Soc.*, 2021, **168**, 010529.

22 T. Yamamoto, K. Matsumoto, R. Hagiwara and T. Nohira, *J. Electrochem. Soc.*, 2021, **168**, 040530.

23 K. Shimoda, T. Minato, H. Konishi, G. Kano, T. Nakatani, S. Fujinami, A. Celik-Kucuk, S. Kawaguchi, Z. Ogumi and T. Abe, *J. Electroanal. Chem.*, 2021, **895**, 115508.

24 X. Li, Y. Tang, J. Zhu, H. Lv, Y. Xu, W. Wang, C. Zhi and H. Li, *Adv. Energy Mater.*, 2021, **11**, 2003714.

25 E. Peled, *J. Electrochem. Soc.*, 1979, **126**, 2047–2051.

26 S. K. Heiskanen, J. Kim and B. L. Lucht, *Joule*, 2019, **3**, 2322–2333.

27 J. Tan, J. Matz, P. Dong, J. Shen and M. Ye, *Adv. Energy Mater.*, 2021, **11**, 2100046.

28 C. M. Julien and A. Mauger, *AIMS Mater. Sci.*, 2018, **5**, 650–698.

29 L. Meyer, N. Saqib and J. Porter, *J. Electrochem. Soc.*, 2021, **168**, 090561.

30 T. Yamanaka, H. Nakagawa, S. Tsubouchi, Y. Domi, T. Doi, T. Abe and Z. Ogumi, *ChemSusChem*, 2017, **10**, 855–861.

31 T. Yamanaka, H. Nakagawa, S. Tsubouchi, Y. Domi, T. Doi, T. Abe and Z. Ogumi, *Electrochim. Acta*, 2017, **234**, 93–98.

32 T. Yamanaka, T. Abe, K. Nishio and Z. Ogumi, *J. Electrochem. Soc.*, 2019, **166**, A635–A640.

33 T. Yamanaka, K. Okazaki, T. Abe, K. Nishio and Z. Ogumi, *ChemSusChem*, 2019, **12**, 527–534.

34 T. Yamanaka, K. Okazaki, Z. Ogumi and T. Abe, *ACS Appl. Energy Mater.*, 2019, **2**, 8801–8808.

35 T. Yamanaka, A. Celik-Kucuk, Z. Ogumi and T. Abe, *ACS Appl. Energy Mater.*, 2020, **3**, 9390–9400.

36 T. Yamanaka, Z. Ogumi and T. Abe, *J. Mater. Chem. A*, 2021, **9**, 22544–22554.

37 Y. Yamada, F. Sagane, Y. Iriyama, T. Abe and Z. Ogumi, *J. Phys. Chem. C*, 2009, **113**, 14528–14532.

38 M. Morita, Y. Asai, N. Yoshimoto and M. Ishikawa, *J. Chem. Soc., Faraday Trans.*, 1998, **94**, 3451–3456.

39 V. Y. Kavun, E. I. Voit, R. M. Yaroshenko and V. K. Goncharuk, *J. Non-Cryst. Solids*, 2014, **401**, 224–231.

40 L. Kumari, J. H. Lin and Y. R. Ma, *J. Phys. D: Appl. Phys.*, 2008, **41**, 025405.

41 A. Reyes-Contreras, M. Camacho-Lopez, S. Camacho-Lopez, O. Olea-Mejia, A. Esparza-Garcia, J. G. Banuelos-Muneton and M. A. Camacho-Lopez, *Opt. Mater. Express*, 2017, **7**, 1777–1786.

42 K. A. Trentelman, *J. Raman Spectrosc.*, 2009, **40**, 585–589.

43 Z. Hong and V. Viswanathan, *ACS Energy Lett.*, 2018, **3**, 1737–1743.

44 Z. Mu, Z. Guo and Y.-H. Lin, *Energy Storage Mater.*, 2020, **30**, 52–58.